Accidental BICs and Chiroptical Response of Hollow-channels in Silicon Nanodisk Resonator-based Metasurfaces for Chiral Sensing

Shubhanshi Sharma,[*,†] Alina Karabchevsky,[‡,¶] and Shailendra K. Varshney[†]

†*Department of Electronics and Electrical Communication Engineering, Indian Institute of Technology Kharagpur, Kharagpur, West Bengal, India, 721302*

‡*School of Electrical and Computer Engineering, Ben-Gurion University of the Negev, Beer-Sheva, 8410501, Israel*

¶*Department of Physics, Lancaster University, LA1 4YB, United Kingdom*

E-mail: shubhanshi07@iitkgp.ac.in

Abstract

Achieving light confinement at the nanoscale is essential for enhancing light-matter interactions, and bound states in the continuum (BICs) have emerged as one of the promising approaches. This study presents a dielectric metasurface design featuring air channels within a silicon nanodisk resonator, demonstrating symmetry-protected BICs (SPBICs) and accidental BICs (ABICs). Here, we report the SPBICs that exhibit an exceptionally high quality (Q) factor at very low asymmetry parameters. An increase in asymmetry decreases the Q-factor quadratically. To alleviate this, we observe that the SPBIC can be transformed into ABICs by adjusting the radius of one air channel that converts the resonances from quasi-SPBICs to quasi-ABICs. Introducing

a third air channel with an optimized radius helps to achieve an ultra-high Q-factor $\approx$ 38000. Multiple ABICs with enhanced local fields were observed for both x- and y-polarizations. The triple air channel design also achieves maximal extrinsic chiral response by breaking the symmetry through an oblique incidence angle, which influences circular dichroism (CD) and transmittance for different circular polarizations. Numerical simulations reveal that the proposed chiral metasurface achieves a near-perfect value of CD $= -0.99$, a Q-factor 8846, and a field enhancement by a factor of 200. Moreover, slightly tilting the nanodisk can realize a high intrinsic chirality (CD $= -0.88$) with a Q-factor $\approx 10^4$. The concept of chiral BICs studied here can be utilized, but not limited to, in applications such as chiral sensing, bio-imaging, and chiroptical spectroscopy.

Keywords

Accidental Bound States in the continuum, Chiral Metasurfaces, Dielectric Metasurfaces, Fano resonances, Circular Dichroism

1 Introduction

The ability to manipulate light-matter interactions at the nanoscale, mainly by controlling amplitude, polarization, and phase,[1,2] is crucial for advancing optical technologies[3] that span a wide range of fundamental sciences.[4] Exploring bound states in the continuum (BIC) enhances field confinement at the nanoscale.[5] The BICs are localized, nonradiative electromagnetic states that exist within the radiation continuum, theoretically resulting in an infinite quality factor (Q) and zero resonance linewidth.[5,6] As a result, they are not detectable in the resonance spectrum unless a symmetry operation is performed. The BICs are generally classified into symmetry-protected BICs (SPBICs) and accidental BICs (ABICs).

The symmetry-protected BICs arise from the preservation of geometrical symmetry with respect to the incident light.[7–9] In contrast, accidental BICs occur when all leakage channels

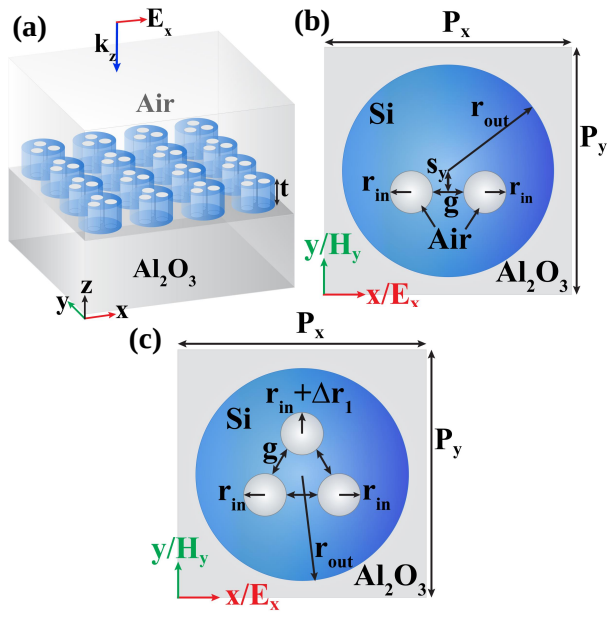

Figure 1: (a) Illustration of an infinite periodic array of the hollow-channels aided Silicon nanodisk resonators metasurface placed on the sapphire substrate. Top view of the unit cell of the nanodisk resonator with (b) two air channels offset in negative y-direction and (c) three air channels placed on equilateral vertices.

have vanished for a specific wavevector in k-space or a particular geometric parameter.[10–12] Both SPBICs and ABICs can be converted into quasi-bound states in the continuum (QBICs) by perturbing the structure, giving rise to either Fano or electromagnetically induced transparency (EIT) resonances or both in the spectrum, with a finite and high Q-factor.[13]

Due to the complexity of introducing an optimum asymmetry, achieving symmetry-protected quasi-BICs (SPQBICs) remains a significant challenge. However, accidental quasi-BICs (AQBICs) are easier to achieve, as they allow for simpler structural designs that are less dependent on symmetry and are more practical for fabrication. The BICs have been demonstrated in various photonic structures, including photonic crystal slabs,[14,15] metamaterials,[16] plasmonic structures,[17,18] hybrid plasmonic-dielectric structures,[19,20] compound waveguide grating structures[21,22] and hybrid waveguide meta structures.[23] These structures are used to enhance various physical processes such as nonlinearity,[24,25] chirality,[26,27] sensing,[28,29] and photon emission.[30,31] It will be noteworthy to combine BICs with chirality, which has tremendous potential to attain maximum optical chirality. Chirality is a common

phenomenon in nature, where an object cannot match its mirror image through symmetry operations such as rotation or translation. It has significant importance across various fields, including optics and photonics,[32,33] material sciences,[34,35] biomedical,[36,37] and drug development.[38,39] Optical chirality arises when a chiral object interacts with the light of a specific helicity while being transparent to the light of the opposite helicity due to variations in amplitude, phase, and polarization. The key measures of optical chirality include circular dichroism (CD), optical rotation, and change in transmission. In natural materials, chirality is typically weak. Therefore, the chiroptical response is either enhanced by geometrically-induced chiral structures, often referred to as intrinsic or extrinsic chirality. A few examples of intrinsically chiral structures are viz. photonic crystals, metamaterials, origami-based metamaterials, three-dimensional nanostructures, and two-dimensional materials, whereas extrinsic chirality can be achieved by changing the incident angle in achiral structures.[40–42] Combining BICs and chirality generates chiral quasi-BIC metasurfaces with improved circular dichroism for intrinsic and extrinsic chirality which can be utilized in applications such as but not limited to, linear and nonlinear chiral sensing, chiral imaging, enantiomer separation, chiral quick response (QR) code.[43–47] Recently, different designs such as notched nanoresonator metasurfaces,[48,49] tilted trapezoidal photonic crystal slabs,[50] air channel embedded nanoresonator metasurfaces,[51,52] height asymmetric metasurfaces,[53] and waveguide grating[54] have been proposed to achieve near perfect intrinsic and extrinsic chirality.

However, designs reported in the literature are mainly driven by SPBIC, where asymmetry plays a significant role. It is known that the Q-factor decreases with an increase in the asymmetry parameter. In order to achieve a high Q-factor, the asymmetry parameter should be relatively small, which may pose challenges in the fabrication. Also, it is noteworthy that the previously mentioned designs lack multiple chiral responses. In this work, we report two simpler designs of metasurfaces, namely (i) nanodisk with two air channels depicting the SP-BICs with a moderate Q-factor and (ii) nanodisk with three air channels where the SPBICs are transformed into AQBIC possessing high Q-factor. The multiple accidental BICs with

high Q-factor are generated for linearly polarized incident light, resulting in maximal multiple extrinsic and intrinsic chiroptical response. The BICs characteristics of the nanodisk resonators with two and three air channels are analyzed through numerical simulations. In the case of the two air channel design, we achieve high-quality factor multiple SPQBICs, with a magnetic dipole, toroidal electric dipole, and quadrupole moments as their primary moments when the air channels are displaced from the center to induce asymmetry. A small value in the asymmetry parameter in the presence of the substrate yields a field enhancement of $\approx 10^3$ and a Q-factor of 10^5 in the dominant mode of the magnetic dipole moment. On the other hand, nanodisk with triple air channels could generate multiple accidental BICs for both x and y-polarized light. In the case of x-polarized light, AQBICs exhibit a high Q-factor of 38000 when all three air channels are of the same radius. Such a metasurface comprised of a nanodisk with three air channels demonstrates a multi-resonant extrinsic chiral response for oblique incidence with a maximum CD $= -0.99$ and a high Q-factor of 8846. Other than the extrinsic chirality, the structure can exhibit high intrinsic chirality (CD $= -0.88$) and a reasonably high Q factor of the order of four when the nanodisk resonators are tilted. The chiroptical response of the nanodisk exhibits the potential to be utilized in chiral sensing, separation of enantiomers, bio-imaging, and chiroptical spectroscopy.

2 Metasurface Designs

The proposed planar metasurface on the x-y plane features an infinite array of periodic Silicon nanodisk resonators arranged in a square lattice. The nanodisk resonators that constitute the metasurface have multiple air channels. The metasurface is defined by specific parameters: period $P_x = P_y$, nanodisk radius r_{out}, height (or thickness) t, individual air-hole radius r_{in}, and separation between two consecutive air-holes g. The entire metasurface, composed of nanodisk resonators, is placed on a sapphire substrate, as illustrated in Figure 1a. We consider two independent nanodisk resonator designs, namely, (i) nanodisk with two air

channels and (ii) nanodisk with three air channels. The air-channel positions are perturbed to observe and study the BICs in these designs. As illustrated in Figure 1b, both air channels are shifted in the negative y-direction from the center of the nanodisk. In contrast, in Figure 1c, the third air channel is introduced with a slightly different radius r_{in} + r_1, forming equilateral vertices. The optimized parameters of the unit cell are $P_x = P_y$ = 820 nm, r_{out} = 370 nm, r_{in} = 80 nm, g = 75 nm, and t = 350 nm, while the parameters s_y and r_1 are considered variable and discussed later. All numerical simulations are performed using COMSOL with periodic boundary conditions in the x and y directions and perfectly matched layers in the z-direction of the unit cell with dispersive Silicon (Si).[55] The refractive index of the substrate (Sapphire) is 1.74.

3 Results and Discussions

3.1 Design 1: Nanodisk with two air channels

The design of two air holes in the nanodisk without any shift in y (i.e., $s_y = 0$) exhibits C_{2v} symmetry. It facilitates symmetry-protected BICs, as evident from eigenmode analysis (see Table S1 in the supplementary information). The refractive index of Silicon is fixed at 3.47, while the substrate is not considered in the eigenmode analysis.

When $s_y \neq 0$ nm, the C_{2v} symmetry changes to C_s because all the rotational and mirror symmetries are broken, except for the mirror plane x = 0. The metasurface for the optimized parameters exhibits eight resonant modes, 1 to 8. Among these, resonant modes 1, 3, 5, 7, 6, and 8 are symmetry-protected BICs. Modes 1, 7, 6, and 8 are identified as SPBIC I, II, III, and IV for ease of reference and marked in the plots. The dominant components of each resonant mode are determined through the Cartesian multipolar decomposition method (CMDM),[56] *viz:* the magnetic dipole (MD) in Mode 1, magnetic quadrupole (MQ) in Modes 3, 7, and 8, and electric quadrupole (EQ) in Mode 6. The dominant multipoles in resonant modes 2, 4, and 5 are the toroidal electric moment (TED).

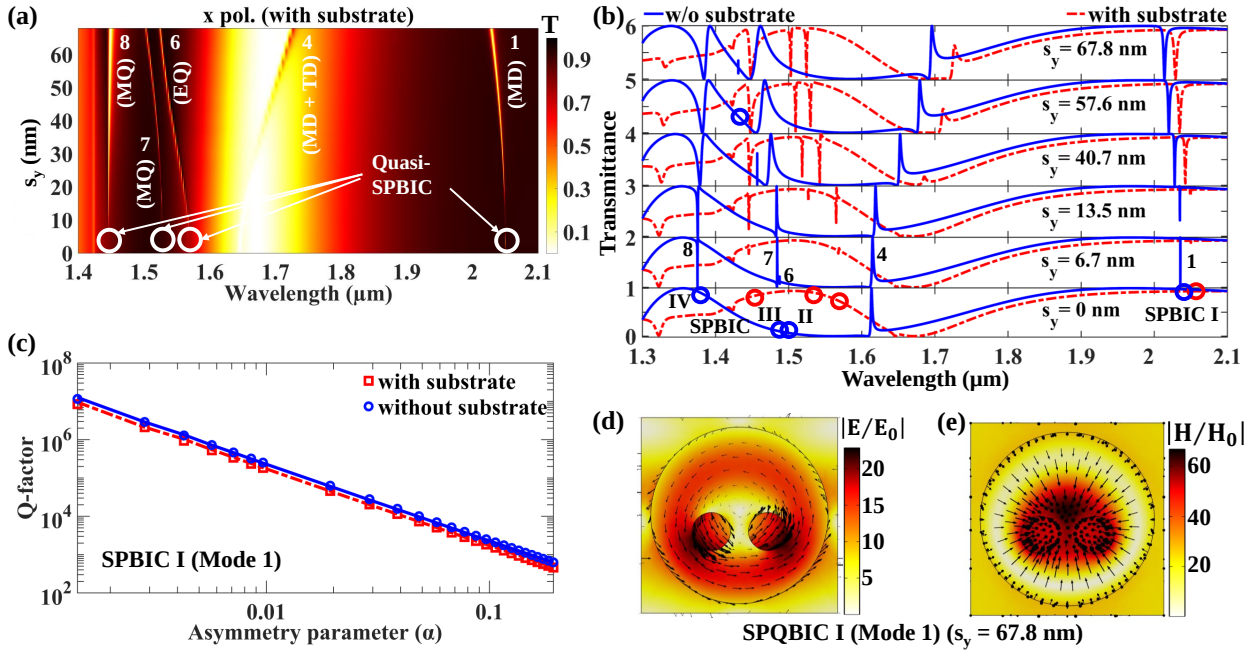

Figure 2: (a) Surface plot illustrating transmittance for various offset values of s_y when the incident light is x-polarized in the presence of substrate. The quasi SPBICs are highlighted with open circles and various modes along with the dominant multipole moments are also marked, (b) Transmittance line spectra for different asymmetry parameter values in both cases with and without substrate, highlighting the SPBICs (blue markers) and SPQBICs (red markers), (c) Q-factor of SPBIC (Mode 1), calculated using the Fano fitting formula. (d) Electric and (e) Magnetic field intensity plots in a xy-plane along with the field vector distributions for SPQBIC (Mode 1) when s_y = 67.8 nm with the substrate.

We introduced in-plane asymmetry to analyze the characteristics of BICs in the transmittance spectra. The QBICs are achieved by displacing the air channels from the center and shifting along the negative y-axis, shown in Figure 2b. The shift of both air channels is achieved by varying the s_y parameter (0 to 67.8 nm). Note that we consider a hypothetical scenario when there is no substrate. For the normal incidence of a plane wave with x polarization, the BIC transforms into QBICs, taking the form of Fano resonances. As depicted in Figure 2a,b, as the shift s_y increases from 0 to 67.8 nm, the structure's symmetry is disrupted, causing the bound states to start interacting with the incoming radiation irrespective of a substrate. Thus, SPQBIC I, II, III, and IV start appearing in transmittance spectra both in the case of without and with the substrate as seen in Figure 2a,b. When the metasurface is placed on the substrate, the mirror symmetry in the z plane is broken, transforming the BICs

to QBICs, along with the redshift of resonances; hence, there is no resonance crossing, as seen in Figure 2a where the SPQBICs are highlighted in white. Whereas in the case without substrate, SPBIC II and SPBIC III experience resonance crossing at $s_y = 13.5$ nm, leading to a swap of resonant modes with an exchange of their position in terms of wavelength. Following the resonance crossing, at around $s_y = 57.6$ nm, the SPBIC II demonstrates accidental BIC, vanishing of resonances in the transmittance spectra, as illustrated in Figure 2b.[57]

To quantitatively assess the level of asymmetry, we define the shift, s_y in terms of the dimensionless asymmetry parameter $= s_y=\sqrt{r_{out}^2 - (r_{in} + 0{:}5g)^2}$ where the parameter's values range from 0 to 1, representing the minimum and maximum shift scenarios. The Q-factor of the modes can be determined as $!_0=$, where is the resonance linewidth obtained using the Fano formula mentioned in equation 1 and fitting the transmittance spectrum. The Fano fitting expression is given as described in[58]

$$T_{fano}(!) = T_0(!) + A_0\frac{(q + 2(! - !_0)=)^2}{1 + (2(! - !_0)=)^2} \tag{1}$$

T_0 is background scattering, w_0 is resonance frequency, q is the Fano parameter, and A_0 is the coupling constant between the bright (continuum state) and dark (discrete state). As the parameter increases, the Q-factor of SPBIC I decreases, as shown in Figure 2c. The primary focus is on SPBIC I and how the introduction of air channels tailors its characteristics. Ideally, when $= 0$, BICs with an infinite Q-factor exist but cannot be observed in the transmittance spectra. The SPBIC I exhibit the maximum quality factor of $1{:}89 \times 10^9$ at $= 0$ for the freestanding structure. In numerical simulations with extremely high resolutions, the Q-factor can reach infinity, thus confirming the existence of a non-radiative BIC. At $= 0.193$ ($s_y = 67.8$ nm), the SPBIC I yields a Q ≈ 650 in the absence of the substrate, while in the presence of the substrate, it is 580. The interaction between SPBIC II and III is characterized by weak coupling. Specifically, the Q-factor of SPBIC II increases compared to SPBIC III, which experiences a decrease in Q-factor as the crossing occurs with an increase in

displacement of air channels from the center, governed by s_y (see supplementary Figure S2). Upon examining symmetry-protected QBICs, the radiative Q-factor demonstrates an inverse quadratic relationship with the asymmetry parameter, , represented as $Q_{rad} = k$ ^{2},[58] where k denotes a proportionality constant. In Figure 2c, the fitted Q-factor of SPBIC I is depicted by square markers, illustrating its adherence to the relationship mentioned above in both the presence and absence of a substrate.

While investigating the quasi-BIC nature of the modes, we can utilize multipolar decomposition to calculate the scattered power through displacement current density in the nanodisk resonator. For SPBIC I, in the absence of a substrate, when air channels are displaced by $s_y = 67.8$ nm, the quasi-BIC emerges at $= 2.013$ m. The CMDM analysis reveals that at quasi-BIC, the z-component of the magnetic dipole moment is dominant, while the other moments are negligible (see supplementary Figure S3), which holds even in the presence of a substrate. Additionally, the near-field distribution in the x-y plane suggests the circular electric field lines and out-of-plane magnetic lines, which lead to the dominant z-component of the magnetic field as shown in Figure 2d,e. It is evident from Figure 2e that there is a significant magnetic field enhancement ($|H/H_0| \approx 67$) when the substrate is present in the case of SPBIC I. The magnetic field enhancement increases in the absence of the substrate (see supplementary Figure S4a,b). The magnetic field becomes highly confined with the decrease in the asymmetry parameter. As an example, for asymmetry, $= 1\%$, the quasi-BIC induces a field enhancement 1000 times (see supplementary Figure S4c,d). Note that in the case of a y-polarized incidence, the metasurface supports resonant modes 3, 4, and 5. Among these, modes 3 and 5 are SPBICs that appear in the transmittance spectra when the air channels are displaced from the center (see supplementary Figure S5).

3.2 Design 2: Three air channels nanodisk resonator

As mentioned earlier, one has to have accurate control of asymmetry parameters to achieve SPBIC with high Q, which poses a fabrication challenge. To alleviate this constraint, we

study the development of accidental BICs, which demonstrate a very high Q-factor and can be achieved with simple design parameters. As observed in the previous section, the Q-factor of SPQBIC decreases quadratically with the increase in asymmetry parameter. Therefore, we modify the nanodisk resonator design by introducing the third air channel in the nanodisk to transform the SPQBIC to AQBIC, where the Q-factor remains high even for a greater degree of structural perturbation. To observe the formation of ABICs, we modified the structure of two air channels in the disk and introduced a third air channel, as depicted in Figure 1c. This design is similar to our earlier work in,[59] where the structure had different dimensions and was placed on a silica substrate. In the current study, we used sapphire as the substrate. The placement of the third air channel inside the disk was such that an imaginary line connecting the center of all air channels formed an equilateral triangle, with its center coinciding with the center of the Si nanodisk. The radius of the third disk was taken as $r_{in} +$ r_1, and the gap (g) between all the air channels is equal, while all other parameters remained the same as above. By increasing or decreasing the r_1, we can control the radius of the third air channel. To achieve optimal accidental BICs, it's crucial to maintain reflection symmetry in the z = 0 plane, as emphasized in.[60] Therefore, the metasurface is considered freestanding in a uniform air environment and illuminated normally with x-polarized and y-polarized light.

3.2.1 x-polarized Incidence

In this subsection, we analyze the metasurface constituted by the nanodisk resonators with triple air channels when the x-polarized plane wave is incident normally. When the radius of the third air channel is changed by r_1, the triple air channel nanodisk resembles two air-channel nanodisk at $r_1 = -80$ nm, corresponding to the situation as $s_y = 67.8$ nm, where all the resonant modes remain the same as that of two air-channels. As r_1 increases, the transmittance spectra in Figure 3b show that the linewidth of resonant mode 1 near $= 2$ m gradually decreases and disappears at $r_1 = 5.6$ nm (indicated by the open circle) in case of no substrate. The resonant mode 1 reappears later with a gradually increasing

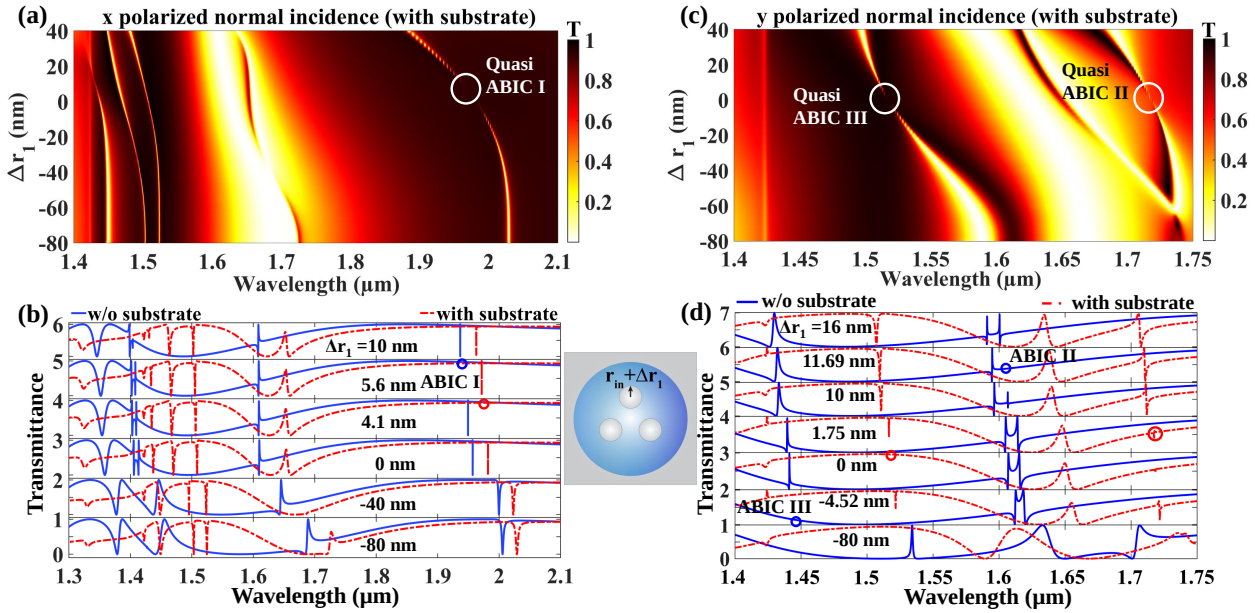

Figure 3: Transmittance under x-polarization (a) surface plot illustrating the formation of AQBIC I (marked by an open circle) in the presence of substrate and (b) line plot of transmittance with and without substrate. Transmittance under y-polarization (c) surface plot indicating AQBIC II and AQBIC III (marked by open circles) in the presence of substrate, and (d) line plot demonstrating the comparison with and without substrate case. The blue and red circles show the formation of ideal ABIC and AQBIC in the case with and without substrate, respectively. The inset shows the unit cell of a nanodisk resonator with three air channels.

linewidth, suggesting the emergence of ABIC I. This assertion can be further supported by examining the Q-factor for ABIC I, obtained through eigenmode analysis and depicted as a function of r_1 in Figure 4a. It is clear that as r_1 approaches 5.6 nm, the Q-factor tends towards infinity and demonstrates an inverse quadratic relationship with r_1. Simulation results are fitted with $Q \propto 1/(r - r_{BIC})^2$, confirming the presence of the ideal ABIC in theory. The presence of the ABIC within the specified framework can be comprehended physically by analyzing the near-field distribution of the electromagnetic field and CMDM.[56] The ABIC I transforms into quasi-ABIC I (AQBIC I) for $r_1 = 10$ nm. From Figure 4b,c, it is evident that the electric field rotates within the xy plane of the nanodisk resonator, resulting in the generation of an out-of-plane magnetic dipole (MD) in the yz plane, while the circulating magnetic field in the yz plane signifies the development of an in-plane elec-

tric dipole (ED). This observation can be corroborated through CMDM analysis. Figure 4d demonstrates that the dominant multipoles consist of out-of-plane MD as well as other out-of-plane magnetic multipoles like MQ and magnetic octupole (MO), along with comparatively weaker in-plane electric multipoles such as EQ, electric octupole (EO), ED, TED, and toroidal electric quadrupole (TEQ). These in-plane electric multipoles and out-of-plane magnetic multipoles combine to generate a TE-polarized wave at a specific geometrical parameter and destructively interfere with each other in the parameter space, as is the case with $r_1 = 5.6$ nm, resulting in the formation of the non-radiating ideal infinite Q-factor ABIC.[61]

We further examine the impact of incorporating the sapphire substrate beneath the metasurface. The substrate introduces an extra leakage channel by breaking the vertical symmetry,[62] leading to the emergence of both odd and even multipoles for a specific resonant mode. Additionally, all resonant modes experience a red shift compared to the scenario without the substrate. As r_1 increases in the metasurface with the substrate, the resonant mode 4 around $= 1.68$ m weakly interacts with the bright background mode and diminishes around $r_1 = -38$ nm, as illustrated in Figure 3a. The increase in r_1 results in the strong coupling of a broad bright mode in the background with the dark Fano resonant mode 4, leading to the formation of EIT,[63,64] as depicted in Figure 3a,b. At $r_1 = 10$ nm, EIT at $= 1.651$ m exhibits a Q-factor of 245. For the resonant mode 1, the resonance becomes narrower as r_1 increases, and the mode disappears around $r_1 = 4.1$ nm (represented by an open circle in Figure 3a,b), indicating the presence of AQBICs. It re-emerges with enhanced linewidth. In the presence of a substrate, the Q-factor has a finite value of 10^5 around $r_1 = 4.1$ nm and displays an inverse quadratic relation with varying r_1. The breaking of vertical symmetry transforms the ideal ABIC into a supercavity mode, resulting in a finite Q-factor value near the vanishing point.

Note that when $r_1 = 10$ nm, resonant mode 1 demonstrates a Q-factor of approximately 44,000 at a wavelength of $= 1.936$ m in the absence of the substrate. Even in the presence

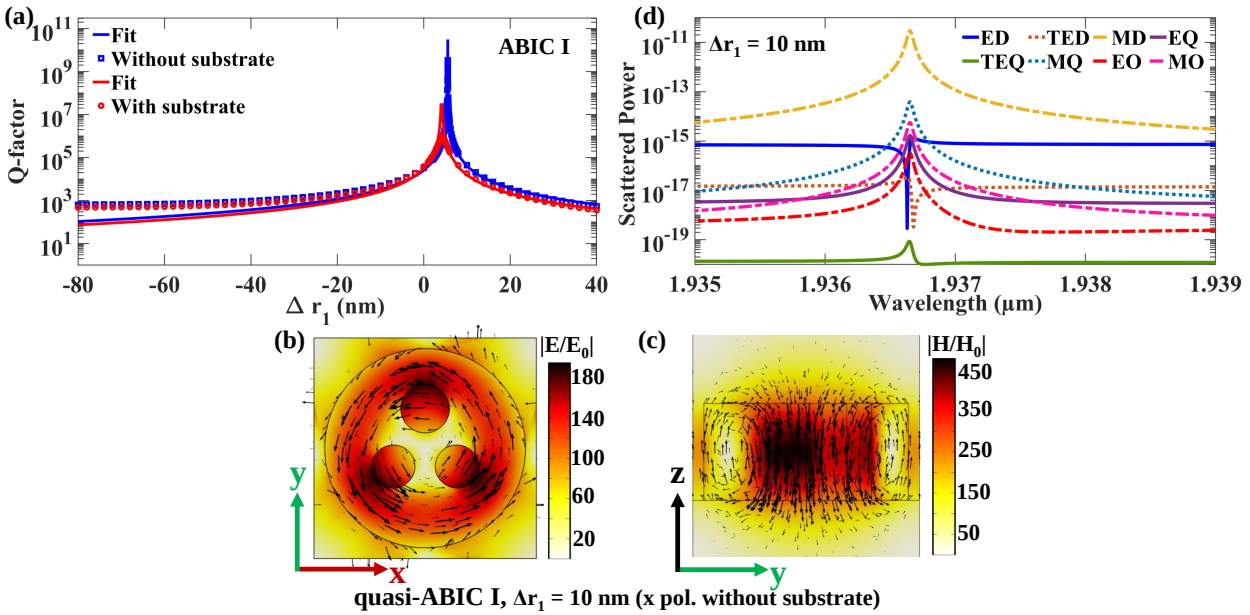

Figure 4: (a) Simulated (marker) and fitted (solid line) Q-factor for the ABIC I with and without substrate. The normalized electric field distribution in the xy-plane is shown in (b), while figure (c) illustrates the normalized magnetic field distribution in the yz-plane. (d) Multipolar distribution plot of AQBIC I when $r_1 = 10$ nm, without substrate. In this context, TEQ, EO, and MO represent toroidal electric quadrupole, electric octupole, and magnetic octupole, respectively.

of the substrate, the Q-factor decreases by a factor of 2.5, possessing a high magnetic field enhancement of $|H{=}H_0| \approx 305$ (see supplementary Figure S6c,d). For $r_1 = 0$ nm, the metasurface with substrate shows a high Q-factor of approximately 38000, resulting in a high magnetic field enhancement ($|H{=}H_0| \approx 504$, see supplementary Figure S6a,b). Furthermore, the nanodisk with the third air channel of radius = 80 nm ($r_1 = 0$ nm) and 90 nm ($r_1 = 10$ nm) is easy to fabricate.

3.2.2 y-polarized Incidence

Similarly, when a plane wave of light polarized in the y-direction interacts with a metasurface composed of nanodisk resonators with three air channels where $r_1 = -80$ nm (resembling two air channels with $s_y = 67.8$ nm with same mode numbers for y-polarized incidence), the standalone metasurface (i.e. without substrate) displays an EIT mode at $= 1.535$ m and two Fano resonances at $= 1.633$ m and $= 1.706$ m with opposite polarities. As

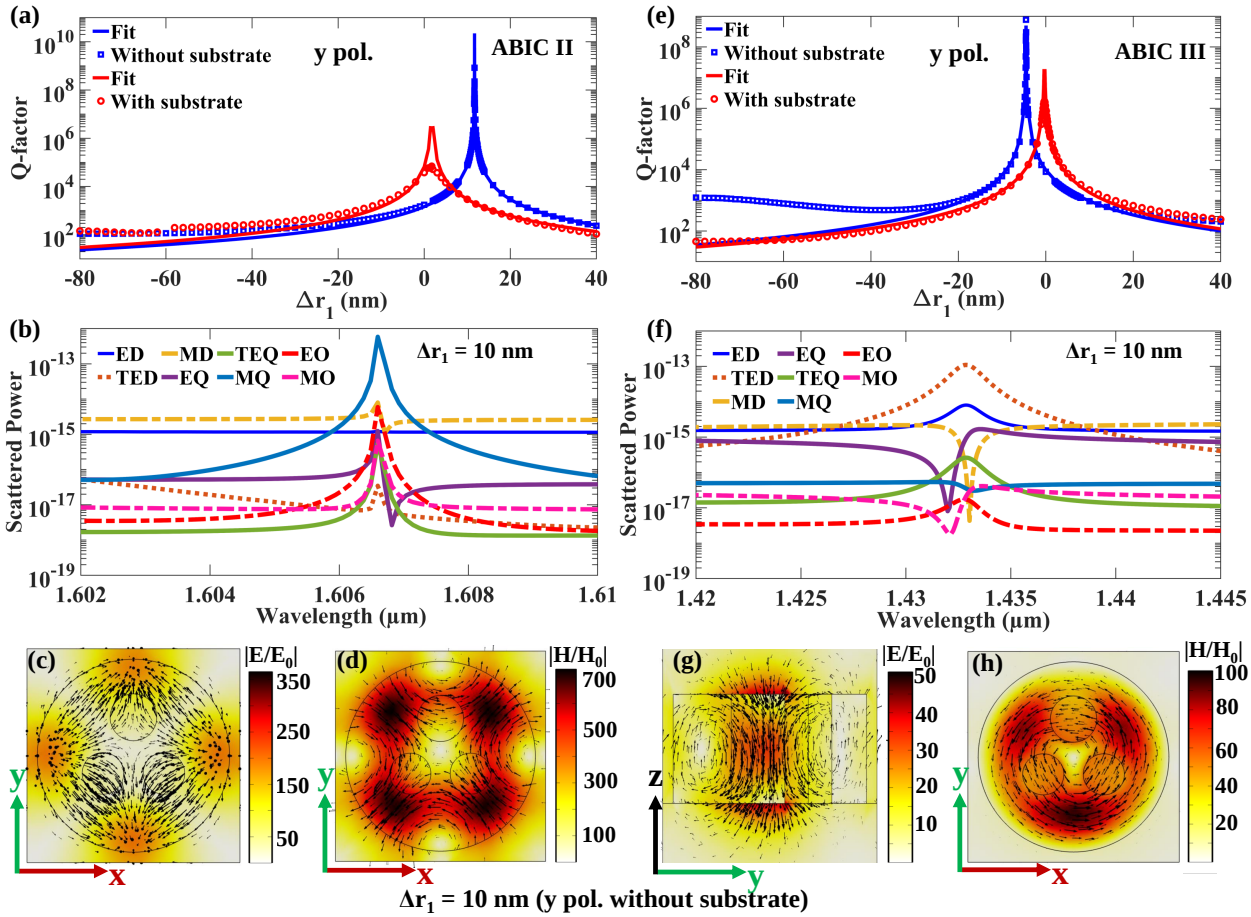

Figure 5: (a) and (e) Depict the simulated Q-factor (marker) and the fitted Q-factor (solid curve) for both ABIC II and ABIC III with and without substrate. The multipolar content when $r_1 = 10$ nm without substrate for (b) AQBIC II and (f) AQBIC III. Normalized electric field distribution (intensity and arrow plot) is shown in (c) xy-plane for AQBIC II and (g) yz-plane for AQBIC III without substrate. Normalized magnetic field intensity and arrow plot distribution in the (d) xy-plane for AQBIC II and (h) xy-plane for AQBIC III without substrate.

the r_1 increases, the Fano resonance close to 1.7 m shifts towards the blue end of the spectrum and weakly interacts with the Fano resonance near 1.6 m. This weak interaction causes the resonances to intersect at $r_1 = -14$ nm. Consequently, at $r_1 = -12$ nm, the destructive interference between the resonances gives rise to a new phenomenon known as EIT at $= 1.623$ m. As r_1 continues to increase, the resonances decouple, leading to the narrowing and eventual disappearance of the resonance at $= 1.606$ m at $r_1 = 11.69$ nm. This disappearance results in the formation of an ideal ABIC II (indicated by an open blue

circle), as shown in Figure 3d. Similarly, at $r_1 = -4.52$ nm, the EIT resonances around $= 1.53$ m vanish, creating an ideal ABIC III. Upon further increasing the r_1 value, we observe the reappearance of quasi-ABIC II (AQBIC II) and quasi-ABIC III (AQBIC III) resonances. Figures 5a,b reveal that the Q-factor tends to approach infinity at $r_1 = 11.69$ nm and $r_1 = -4.52$ nm for both ABIC II and ABIC III, respectively. Additionally, the Q-factor demonstrates an inverse quadratic relationship with r_1, indicating the presence of ideal ABIC. The origins of ABIC II and ABIC III can be comprehended through multipolar decomposition and the near-field intensity distribution.

For $r_1 = 10$ nm, AQBIC II demonstrates a quadrupolar nature in the xy-plane as shown in Figure 5c,d, with magnetic quadrupole to be the dominant multipole (Figure 5b). At the same time, AQBIC III arises due to the resonance's toroidal nature. The analysis of Figure 5g reveals that in the yz-plane, the electric dipole aligns along the z-axis while the magnetic field circulates in the xy-plane, resulting in the generation of a magnetic dipole along the x-axis (Figure 5h). Consequently, the toroidal moment is produced along the z-axis. That is further supported by Figure 5f, where the dominant multipole is identified as TED. Thus, ABIC III can be identified as accidental BIC resulting from the destructive interference of TED, ED, MQ, and other weak multipoles such as EQ and MD.

We learned from the x-polarized incidence that introducing a substrate beneath the metasurfaces causes the resonances to red-shift and disrupts the vertical symmetry of the structure, resulting in the transformation of the ideal ABIC to AQBIC. Consequently, in the presence of the substrate, when $r_1 = -80$ nm, EIT is observed at $= 1.613$ m, while the other two resonances are weakly linked around $= 1.735$ m. Moreover, resonance crossing occurs at $r_1 = -68$ nm, leading to the emergence of EIT at $r_1 = -60$ nm at $= 1.735$ m. The intensity of EIT increases, and it acquires the Fano lineshape, as depicted in Figure 3c,d. With a further increase in the parameter r_1, the Fano resonance at approximately 1.72 m and resonance at 1.54 m display AQBIC behavior at $r_1 = 1.75$ nm and $r_1 =$ 0 nm (indicated by white and red open circles in Figure 3c,d).

In a practical scenario involving a substrate, both AQBIC II and AQBIC III exhibit finite Q-factor at $r_1 = 1.75$ nm and $r_1 = 0$ nm, respectively. At $r_1 = 0$ nm , the resonances have a Q-factor of 37845 for AQBIC II and $8{:}90 \times 10^5$ for AQBIC III, accompanied by the magnetic field enhancement, $|H{=}H_0|$ of 280 and 2098, and electric field enhancement, $|E{=}E_0|$ of 162 and 1530, respectively (see supplementary Figure S7a,b and Figure S8a,b). Meanwhile, at $r_1 = 10$ nm , the resonances exhibit Q-factors of 2950 for AQBIC II and 2170 for AQBIC III, with magnetic field enhancements, $|H{=}H_0|$ of 135 and 131, and electric field enhancements, $|E{=}E_0|$ of 78 and 93, respectively (see supplementary Figure S7c,d and Figure S8c,d).

4 Chirality in hollow air channels nanodisk resonator

In this section, we study the chiroptical response of the hollow-air channels aided metasurface, both extrinsic and intrinsic chirality. In order to understand the chiral response, we analyze $e^{\ i!t}$, a time-dependent wave propagating in the negative z direction, which represents circularly polarized light as $1{=}\sqrt{2}(E_x \pm iE_y)$. Here, $+$ denotes right circularly polarized light (RCP), while $-$ indicates left circularly polarized light (LCP). The chirality is determined by circular dichroism, which is defined as the difference between the transmittance of RCP and LCP incidences:[49]

$$CD = \frac{(T_{rr} + T_{lr}) - (T_{ll} + T_{rl}))}{(T_{rr} + T_{lr}) + (T_{ll} + T_{rl})} \tag{2}$$

where, r represents RCP and l represents LCP, respectively.

Firstly, we analyze extrinsic chirality in a nanodisk with two air channels for SPBIC I (see supplementary Figure S9) where it is found that for an incidence angle of $_{in} = 22$, a dip appears in transmittance spectrum for LCP light, $T_{ll} = 0.045$ at 2.086 m. Also, the transmittance of RCP is, $T_{rr} = 0.55$ along with nearly equal cross-polarized components, T_{lr} $= 0.17$ and $T_{rl} = 0.15$ that results in maximum chirality, CD = 0.57 and Q-factor = 641. It

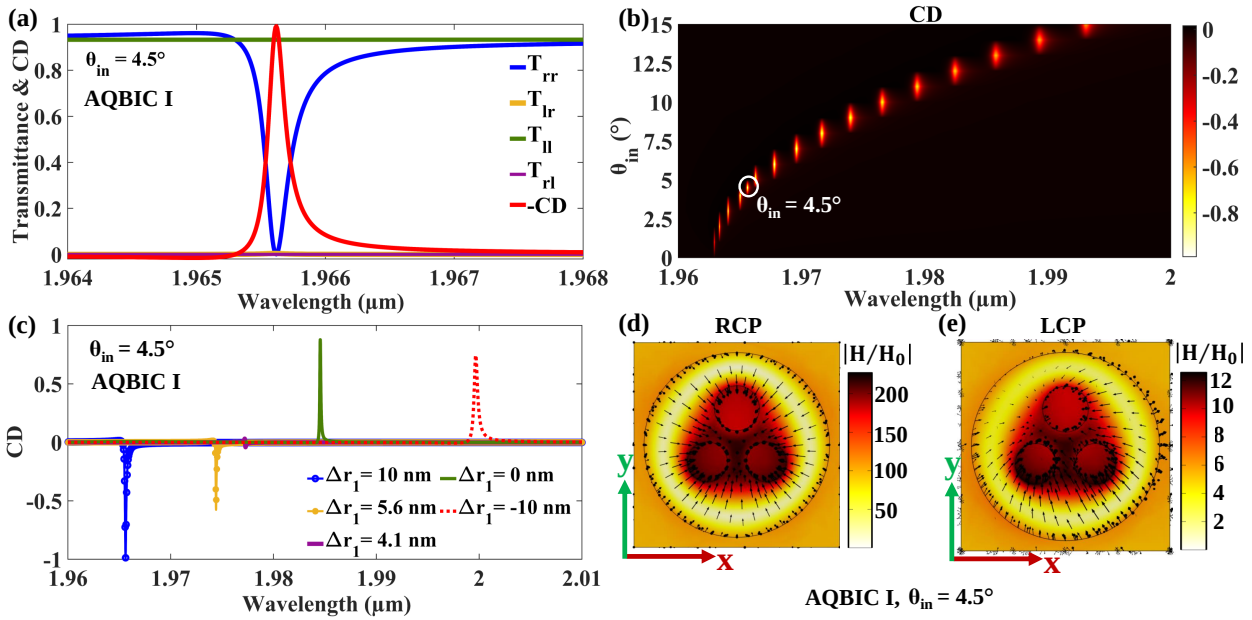

Figure 6: Extrinsic chiroptical characteristics of AQBIC I of nanodisk with three air channels under oblique incidence. (a) Transmittance plot (T_{rr}, T_{lr}, T_{ll}, T_{rl}) and $-$CD when $r_1 = 10$ nm and $_{in} = 4.5$, (b) variation of CD for transmitted waves under various incident angles at a fixed $r_1 = 10$ nm. (c) The CD at a fixed angle of incidence $_{in} = 4.5$ while the r_1 varies. The near magnetic field distribution of the chiral AQBIC resonance in xy-plane for (d) RCP and (e) LCP incidence.

can be inferred that incoming LCP light strongly couples with the nanostructure, but the same is true for the RCP along with their cross-polarization component, which reduces the overall chirality of the system. This is also supported by the electric and magnetic field plots at resonance wavelength, where the field enhancement in both RCP and LCP is weak and is in the order of one. However, it is possible to enhance the extrinsic chirality by breaking the symmetry, i.e., a nanodisk with three air channels.

As discussed earlier, the nanodisk with three air channels demonstrates mirror symmetry along the yz plane. This symmetry persists even when the radius (r_1) varies. Consequently, the structure displays achiral behavior under normal incidence of circularly polarized light. To demonstrate chiral response, all mirror symmetries present in the structure are broken by changing the angle of incidence, i.e., oblique incident. The angle of incidence, $_{in}$, lies in the xz-plane between the incident light and the z-axis, resulting in the breaking of mirror symmetry in the yz-plane as well as the out-of-plane mirror symmetry.[65] Therefore, combining

an achiral metasurface with an oblique incidence creates a chiral AQBIC metasurface.

In the case of AQBIC I, when circularly polarized light is incident at an angle of $_{in} = 4.5$ and $r_1 = 10$ nm, it can be observed from Figure 6a that a resonant dip occurs at 1.9656 m for the RCP co-polarized transmittance, T_{rr}. At the same time, the LCP co-polarized transmittance, T_{ll}, remains close to 0.92. Additionally, the cross-polarized transmittance components, T_{lr} and T_{rl}, are negligible and are less than 0.05 within the resonance range, resulting in a giant CD of about -0.99 and a Q-factor of 8846. In Figure 6b, it is evident that as $r_1 = 10$ nm, the circular dichroism increases and reaches its maximum at $_{in}$ of 4.5 , after which it decreases with the increase in incident angle. It indicates that incident angle less than and greater than 4.5 result in weaker chirality. The structure transmits the LCP light while the RCP light is reflected. The magnetic field intensity plot depicted in Figure 6d illustrates a considerable enhancement of magnetic field confinement by a factor exceeding 200 under RCP illumination. In contrast, it is notably weaker under LCP illumination (Figure 6e). Here, the out-of-plane magnetic field distribution from Figure 6d confirms the dominance of MD moment, which is consistent with the observation made from the multipole decomposition of AQBIC I for x-polarized illumination. The planar design employed here facilitates maximum chirality even with varying r_1, as evident from Figure 6c. When circularly polarized light is incident at $_{in} = 4.5$ and r_1 is varied, a negative value of circular dichroism is observed for positive r_1, indicating coupling between RCP and AQBIC, while LCP remains isolated. Conversely, a decrease in r_1 results in a positive value of CD, indicating coupling between LCP and AQBIC, while RCP is suppressed.

It is noticed that both the AQBIC II and AQBIC III resonances can also exhibit giant extrinsic chirality at $r_1 = 10$ nm, similar to extrinsic chirality in AQBIC I. Figure 7a,b illustrates the extrinsic chirality induced in metasurface when circularly polarized light is incident at an oblique angle. In the case of AQBIC II (7a), the metasurface exhibits a giant chirality of -0.97 at $_{in} = 1$, whereas AQBIC III reveals a high chiral response of -0.98 for $_{in} = 1.5$. The AQBIC II and III yield a Q-factor of 2114 and 894, respectively. As

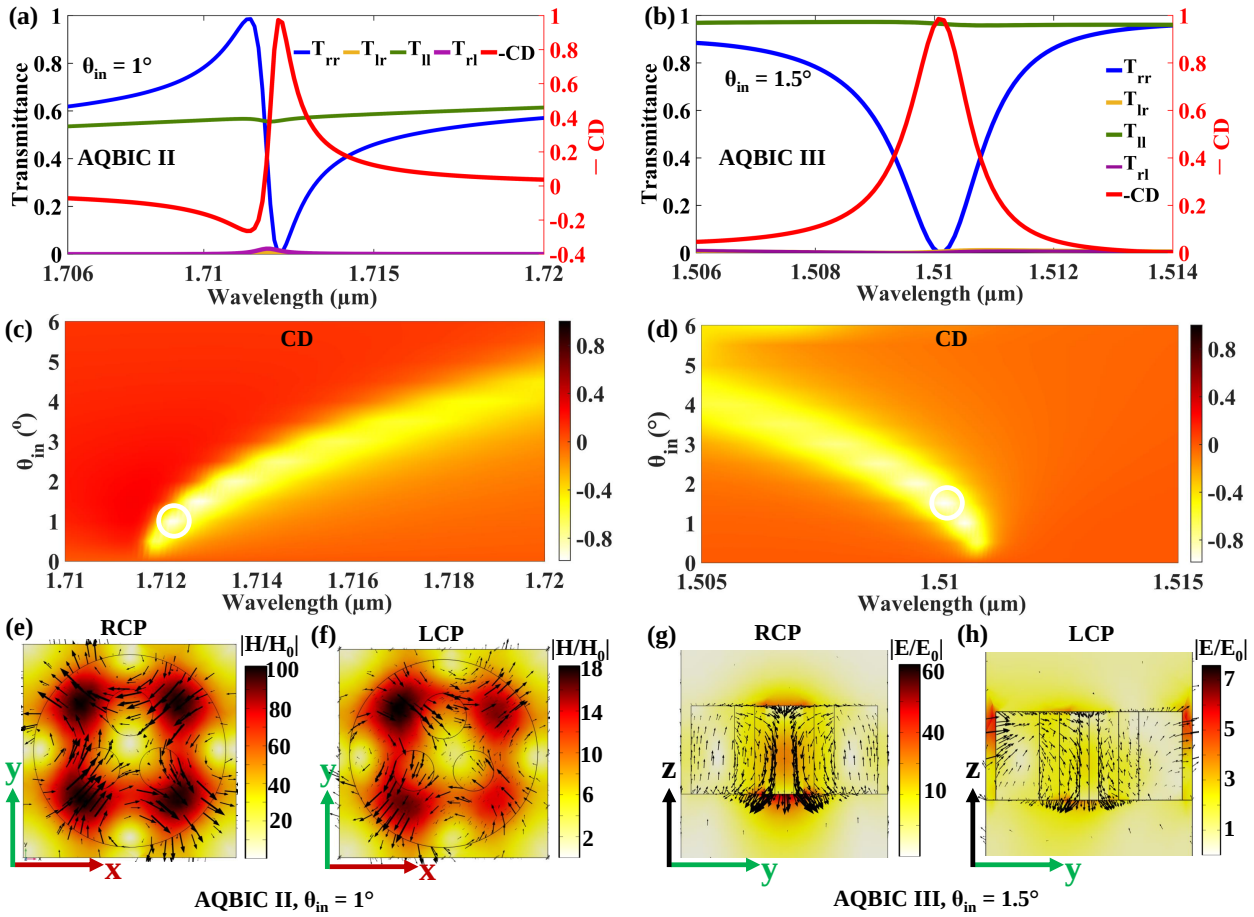

Figure 7: Extrinsic chiroptical characteristics of AQBIC II and III of nanodisk with three air channels at oblique incidence. Transmittance plot (T_{rr}, T_{lr}, T_{ll}, T_{rl}) and −CD when r_1 = 10 nm and (a) $_{in} = 1$ for AQBIC II and (b) $_{in} = 1.5$ for AQBIC III. Variation of CD for transmitted waves at $r_1 = 10$ nm for varying angle of incidence for (c) AQBIC II and (d) AQBIC III. The near magnetic field distribution of the chiral AQBIC II resonance in xy-plane for (e) RCP and (f)LCP incident light. The near electric field distribution of the chiral AQBIC III resonance in yz-plane for (g) RCP and (h) LCP incident light.

the angle of incidence varies while r_1 fixed at 10 nm, in both the cases of AQBIC II and AQBIC III, we observe that CD has its maxima at 1 and 1.5 and decreases before and after this incident angles (Figure 7c,d). This implies the weaker coupling of LCP with the AQBICs. The chiral AQBIC II and AQBIC III resonant modes exhibit MQ and TED nature, as observed from near magnetic and electric field intensity and arrow plot shown in Figure 7e-h. Since RCP is strongly coupled to the resonant modes, we can observe high magnetic and electric field enhancement of 100 and 60 for chiral AQBIC II and AQBIC III from Figure

7e,g, whereas in the case of the LCP, the resonant modes have reduced magnetic and electric field enhancement that can be observed from Figure 7f,h.

It is important to know that an ultra-high Q-factor chiral response can be achieved for AQBIC I, II, and III for certain values of r_1 and $_{in}$, but at the expense of non-unity CD. To illustrate this, r_1 and $_{in}$ are varied for AQBIC I mode, where the Q-factor is ≈ 19519 but CD value is reduced to ≈ 0.94 when $r_1 = 0$ nm and $_{in} = 3.1$. Similarly, for $r_1 = 5.6$ nm and $_{in} = 1.35$, an ultra-high Q-factor $\approx 10^5$ is observed, however CD degrades and come to ≈ -0.86 (see supplementary Figure S10).

This study is not only limited to the observation of extrinsic chiral response by varying the angle of incidence but also studies the intrinsic response of the nanostructure by manipulating the structural design in such a manner that the symmetries that were present earlier in the case of extrinsic chirality vanish. One of the possible approaches to attain intrinsic chirality in the proposed metasurface is to introduce a tilt ($_{tilt}$) in the nanodisk resonator, as shown in the inset of Figure 8a. All the geometrical parameters remain the same, with $r_1 = 10$ nm. Note that, earlier, the center of the nanodisk with three air channels was concentric to the square lattice, which is now shifted in the x-axis by 33 nm to accommodate the tilt angle till $_{tilt} = 10.5$.

The introduction of the tilt in the geometry breaks the out-of-plane symmetry and in-plane symmetry; in this case, symmetry in the yz-plane makes the structure intrinsically chiral. It is observed from Figure 8a that for $_{tilt} = 10.5$ and normal incidence, the metasurface composed of titled nanodisks strongly couples with the RCP, yielding a dip in transmittance spectra, whereas it weakly couples with the LCP such that the LCP is transmitted through the nanostructure. The CD is negligible when the $_{tilt} = 0$. As the $_{tilt}$ increases, the CD also increases, signifying the coupling of the metasurface with the one polarization component. A maximum CD ($= -0.88$) and Q-factor, ≈ 12300 has been achieved for $_{tilt} = 10.5$. Similarly, in the case of AQBIC II, when the nanodisk tilt increases till $_{tilt} = 6$, CD increases, after which CD starts decreasing as seen from Figure 8d. However, we observe

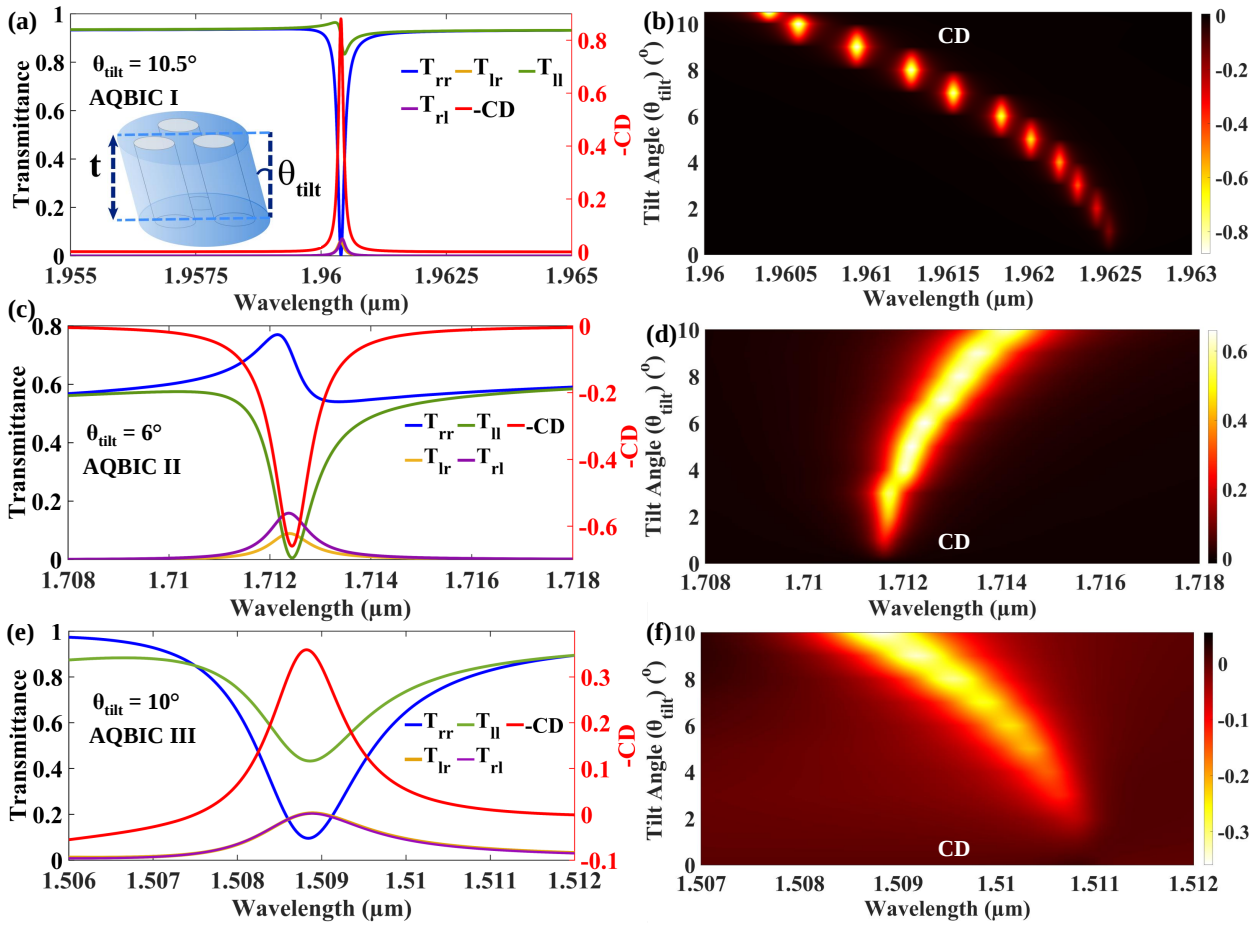

Figure 8: Intrinsic chiroptical characteristics of AQBIC I, II and III of tilted nanodisk with three air channels at normal incidence. Transmittance plot (T_{rr}, T_{lr}, T_{ll}, T_{rl}) and $-$CD when $r_1 = 10$ nm and (a) $_{tilt} = 10.5$ for AQBIC I. Inset shows the schematic of geometrical manipulation of the hollowed nanodisk to realize intrinsic chirality, (c) $_{tilt} = 6$ for AQBIC II and (e) $_{in} = 10$ for AQBIC III. Variation of CD for transmitted waves at $r_1 = 10$ nm for varying tilt angle ($_{tilt}$) for (b) AQBIC I, (d) AQBIC II and (f) AQBIC III.

that the metasurface strongly interacts with the LCP and weakly with the RCP while cross-polarized components are present (see Figure 8c), which is different from the intrinsic chiral response of AQBIC I and AQBIC III. The AQBIC II exhibits a CD = 0.65 with Q-factor = 1691 for $_{tilt} = 6$. In the case of AQBIC III, the intrinsic chiral response is not very strong, as observed from Figure 8e,f. The CD reaches a maximum value of -0.35 and Q-factor 985 as the $_{tilt}$ increases. Figure S11 in the supplementary depicts the near-field distribution in the designed tilted metasurface exhibiting intrinsic chirality for AQBIC I-III.

Based on the analysis, it can be inferred that the nanodisk with the three air channels

transmits the LCP light while the RCP light is reflected. This suggests that precise incident angle adjustment facilitates efficient coupling of AQBICs with the RCP but not with the LCP in case of extrinsic chirality[66] with a near-unity CD of high Q-factor. In the case of intrinsic chirality for a specific tilt angle, AQBIC I and AQBIC III exhibit chirality such that LCP is transmitted and RCP is reflected, but in the case of AQBIC II, RCP is transmitted while LCP is reflected. Therefore, these findings emphasize the maximum chiroptical response to the changes in incident angle and geometric asymmetries and modifications.

In Table S2 (see supplementary information), we have summarized recent work on the chiral quasi-BIC metasurfaces on the basis of type of BICs, number of resonant modes, Q-factors, and CDs and compared it to the work presented in this paper. Clearly, most of the work is done in intrinsic chirality with a high Q-factor and CD utilizing the concept of SPBICs. In comparison to the existing works, our work highlights multiple AQBIC with a high intrinsic and extrinsic chiroptical response (near unity CD and high Q-factor).

5 Conclusion

To summarize, we have demonstrated the incorporation of air channels within nanodisk resonator-based dielectric metasurfaces to enable multiple symmetry-protected and accidental BICs, depending on the design configuration. Specifically, a design with three air channels enables accidental BICs for both x- and y-polarized light by tuning the radius of the third air channel. Additionally, we explored the numerical behavior of achiral metasurfaces with yz-plane symmetry, capable of supporting AQBICs and displaying a strong extrinsic chiroptical response by breaking mirror symmetry under oblique incidence. The strong intrinsic chirality is also exhibited by tilting the nanodisk. By integrating multiple air channels into Si nanodisks, we achieved enhanced multispectral chirality, resonance tunability, a high Q-factor, and significant field enhancement with minor parameter adjustments while maintaining fabrication simplicity. The potential applications of these chiral metasurfaces include chiral

sensing, chiral spectroscopy, spin-selective imaging and optical devices, and nonlinear optics. Beyond BICs, the metasurfaces also support EIT resonances, offering promising avenues for slow-light applications.

Acknowledgement

The authors acknowledge the technical discussions with Monica Pradhan, School of Nanoscience and Technology, Indian Institute of Technology, Kharagpur. This research was supported by the DST Govt. of India, vide no: DST/INT/ISR/P-34/2023 and SPARC/2024-2025/NXTG/P3840 by the Ministry of Education Govt. of India.

Supporting Information Available

The following supporting information is available free of charge.

- Section S1: Eigenmode analysis of and radiation pattern of two air-channels nanodisk resonator
- Section S2: Quality factor of three SPBIC for x-polarization incidence
- Section S3: Multipole decomposition of all the modes for x-polarization incidence in nanodisk with two air channels
- Section S4: Electric and magnetic field plot in nanodisk with two air channels
- Section S5: Transmittance and quality factor plots for two air-channel nanodisk resonator metasurface for y-polarization incidence
- Section S6: Electric and magnetic field plot in nanodisk with three air channels for ABIC I, ABIC II, and ABIC III in case of substrate
- Section S7: Extrinsic chirality in SPBIC I in nanodisk with two air channels

- Section S8: Extrinsic chirality in ABIC I in nanodisk with three air channels for varying r_1
- Section S9: Field plots in tilted nanodisk with three air channels for intrinsic chirality when $r_1 = 10$ nm for AQBIC I, II, and III.
- Section S10: Comparative table depicting the advantages of the current work

References

(1) Kamali, S. M.; Arbabi, E.; Arbabi, A.; Faraon, A. A review of dielectric optical metasurfaces for wavefront control. *Nanophotonics* 2018, *7*, 1041–1068.

(2) Sharma, S.; Pradhan, M.; Yadav, A.; Varshney, S. K. Visible to Infrared Dielectric Metasurfaces and their Applications. *Indian Journal of Pure & Applied Physics (IJPAP)* 2023, *61*, 568–588.

(3) Kuznetsov, A. I. et al. Roadmap for Optical Metasurfaces. *ACS Photonics* 2024, *11*, 816–865, PMID: 38550347.

(4) Chen, H.-T.; Taylor, A. J.; Yu, N. A review of metasurfaces: physics and applications. *Reports on Progress in Physics* 2016, *79*, 076401.

(5) Azzam, S. I.; Kildishev, A. V. Photonic Bound States in the Continuum: From Basics to Applications. *Advanced Optical Materials* 2021, *9*, 2001469.

(6) Hsu, C. W.; Zhen, B.; Stone, A. D.; Joannopoulos, J. D.; Soljačić, M. Bound states in the continuum. *Nature Reviews Materials* 2016, *1*, 1–13.

(7) Zhou, C.; Huang, L.; Jin, R.; Xu, L.; Li, G.; Rahmani, M.; Chen, X.; Lu, W.; Miroshnichenko, A. E. Bound States in the Continuum in Asymmetric Dielectric Metasurfaces. *Laser & Photonics Reviews* 2023, *17*, 2200564.

(8) Zhou, Q.; Fu, Y.; Huang, L.; Wu, Q.; Miroshnichenko, A.; Gao, L.; Xu, Y. Geometry symmetry-free and higher-order optical bound states in the continuum. *Nature Communications* 2021, *12*, 4390.

(9) van Hoof, N. J.; Abujetas, D. R.; ter Huurne, S. E.; Verdelli, F.; Timmermans, G. C.; Sánchez-Gil, J. A.; Rivas, J. G. Unveiling the Symmetry Protection of Bound States in the Continuum with Terahertz Near-Field Imaging. *ACS Photonics* 2021, *8*, 3010–3016.

(10) Li, Z.; Zhou, L.; Liu, Z.; Panmai, M.; Li, S.; Liu, J.; Lan, S. Modifying the Quality Factors of the Bound States in the Continuum in a Dielectric Metasurface by Mode Coupling. *ACS Photonics* 2023, *10*, 206–216.

(11) Abujetas, D. R.; Olmos-Trigo, J.; Sánchez-Gil, J. A. Tailoring Accidental Double Bound States in the Continuum in All-Dielectric Metasurfaces. *Advanced Optical Materials* 2022, *10*, 2200301.

(12) Bogdanov, A. A.; Koshelev, K. L.; Kapitanova, P. V.; Rybin, M. V.; Gladyshev, S. A.; Sadrieva, Z. F.; Samusev, K. B.; Kivshar, Y. S.; Limonov, M. F. Bound states in the continuum and Fano resonances in the strong mode coupling regime. *Advanced Photonics* 2019, *1*, 016001.

(13) Koshelev, K.; Bogdanov, A.; Kivshar, Y. Meta-optics and bound states in the continuum. *Science Bulletin* 2019, *64*, 836–842, SPECIAL TOPIC: Electromagnetic Metasurfaces: from Concept to Applications.

(14) Yang, Y.; Peng, C.; Liang, Y.; Li, Z.; Noda, S. Analytical Perspective for Bound States in the Continuum in Photonic Crystal Slabs. *Phys. Rev. Lett.* 2014, *113*, 037401.

(15) Gansch, R.; Kalchmair, S.; Genevet, P.; Zederbauer, T.; Detz, H.; Andrews, A. M.; Schrenk, W.; Capasso, F.; Lončar, M.; Strasser, G. Measurement of bound states in the

continuum by a detector embedded in a photonic crystal. *Light: Science & Applications* 2016, *5*, e16147–e16147.

(16) Yang, Y.; Jung, W.; Hur, C.; Kim, H.; Shin, J.; Choi, M.; Rho, J. Angle-Resolved Polarimetry with Quasi-Bound States in the Continuum Plasmonic Metamaterials via 3D Aerosol Nanoprinting. *ACS Nano* 2024, *18*, 12771–12780, PMID: 38708928.

(17) Liang, Y.; Koshelev, K.; Zhang, F.; Lin, H.; Lin, S.; Wu, J.; Jia, B.; Kivshar, Y. Bound States in the Continuum in Anisotropic Plasmonic Metasurfaces. *Nano Letters* 2020, *20*, 6351–6356, PMID: 32479094.

(18) Aigner, A.; Tittl, A.; Wang, J.; Weber, T.; Kivshar, Y.; Maier, S. A.; Ren, H. Plasmonic bound states in the continuum to tailor light-matter coupling. *Science Advances* 2022, *8*, eadd4816.

(19) Joseph, S.; Sarkar, S.; Khan, S.; Joseph, J. Exploring the Optical Bound State in the Continuum in a Dielectric Grating Coupled Plasmonic Hybrid System. *Advanced Optical Materials* 2021, *9*, 2001895.

(20) Son, H.; Choi, T.; Kim, K.; Kim, Y.; Bang, J.; Kim, S.-J.; Lee, B.; Jeong, Y. Strong Coupling Induced Bound States in the Continuum in a Hybrid Metal–Dielectric Bilayer Nanograting Resonator. *ACS Photonics* 2024, *11*, 3221–3231.

(21) Wu, F.; Wu, J.; Guo, Z.; Jiang, H.; Sun, Y.; Li, Y.; Ren, J.; Chen, H. Giant Enhancement of the Goos-Hänchen Shift Assisted by Quasibound States in the Continuum. *Phys. Rev. Appl.* 2019, *12*, 014028.

(22) Wu, F.; Liu, D.; Xiao, S. Bandwidth-tunable near-infrared perfect absorption of graphene in a compound grating waveguide structure supporting quasi-bound states in the continuum. *Opt. Express* 2021, *29*, 41975–41989.

(23) Jeon, D.; Rho, J. Quasi-Trapped Guided Mode in a Metasurface Waveguide for Independent Control of Multiple Nonlocal Modes. *ACS Photonics* **2024**, *11*, 703–713.

(24) Koshelev, K.; Kruk, S.; Melik-Gaykazyan, E.; Choi, J.-H.; Bogdanov, A.; Park, H.-G.; Kivshar, Y. Subwavelength dielectric resonators for nonlinear nanophotonics. *Science* **2020**, *367*, 288–292.

(25) Koshelev, K.; Tang, Y.; Li, K.; Choi, D.-Y.; Li, G.; Kivshar, Y. Nonlinear Metasurfaces Governed by Bound States in the Continuum. *ACS Photonics* **2019**, *6*, 1639–1644.

(26) Chen, Y.; Zhao, C.; Zhang, Y.; Qiu, C.-w. Integrated Molar Chiral Sensing Based on High-Q Metasurface. *Nano Letters* **2020**, *20*, 8696–8703, PMID: 33215497.

(27) Gorkunov, M. V.; Antonov, A. A.; Kivshar, Y. S. Metasurfaces with Maximum Chirality Empowered by Bound States in the Continuum. *Phys. Rev. Lett.* **2020**, *125*, 093903.

(28) Romano, S.; Zito, G.; Torino, S.; Calafiore, G.; Penzo, E.; Coppola, G.; Cabrini, S.; Rendina, I.; Mocella, V. Label-free sensing of ultralow-weight molecules with all-dielectric metasurfaces supporting bound states in the continuum. *Photon. Res.* **2018**, *6*, 726–733.

(29) Romano, S.; Mangini, M.; Penzo, E.; Cabrini, S.; De Luca, A. C.; Rendina, I.; Mocella, V.; Zito, G. Ultrasensitive Surface Refractive Index Imaging Based on Quasi-Bound States in the Continuum. *ACS Nano* **2020**, *14*, 15417–15427, PMID: 33171041.

(30) Yang, Y.; Massuda, A.; Roques-Carmes, C.; Kooi, S. E.; Christensen, T.; Johnson, S. G.; Joannopoulos, J. D.; Miller, O. D.; Kaminer, I.; Soljačić, M. Maximal spontaneous photon emission and energy loss from free electrons. *Nature Physics* **2018**, *14*, 894–899.

(31) Son, C.; Sultanov, V.; Santiago-Cruz, T.; Anthur, A. P.; Zhang, H.; Paniagua-Dominguez, R.; Krivitsky, L.; Kuznetsov, A. I.; Chekhova, M. V. Photon pairs bidirectionally emitted from a resonant metasurface. *Nanoscale* **2023**, *15*, 2567–2572.

(32) Wang, M.; Li, H.; Xu, T.; Li, G.; Yu, M.; Jiang, B.; Xu, J.; Wu, J. Probing a chiral drug using long period fiber gratings. *Opt. Express* **2019**, *27*, 31407–31417.

(33) Ma, S.; Ahn, J.; Moon, J. Chiral Perovskites for Next-Generation Photonics: From Chirality Transfer to Chiroptical Activity. *Advanced Materials* **2021**, *33*, 2005760.

(34) Yan, B. Structural Chirality and Electronic Chirality in Quantum Materials. *Annual Review of Materials Research* **2024**, *54*, 97–115.

(35) Jia, S.; Tao, T.; Xie, Y.; Yu, L.; Kang, X.; Zhang, Y.; Tang, W.; Gong, J. Chirality Supramolecular Systems: Helical Assemblies, Structure Designs, and Functions. *Small* **2024**, *20*, 2307874.

(36) Sun, M.; Wang, X.; Guo, X.; Xu, L.; Kuang, H.; Xu, C. Chirality at nanoscale for bioscience. *Chem. Sci.* **2022**, *13*, 3069–3081.

(37) Wang, Y.; Tay, A. Advances in Enantiomer-Dependent Nanotherapeutics. *ACS Nano* **2023**, *17*, 9850–9869, PMID: 37267453.

(38) Ceramella, J.; Iacopetta, D.; Franchini, A.; De Luca, M.; Saturnino, C.; Andreu, I.; Sinicropi, M. S.; Catalano, A. A Look at the Importance of Chirality in Drug Activity: Some Significative Examples. *Applied Sciences* **2022**, *12*.

(39) McVicker, R. U.; O'Boyle, N. M. Chirality of New Drug Approvals (2013–2022): Trends and Perspectives. *Journal of Medicinal Chemistry* **2024**, *67*, 2305–2320, PMID: 38344815.

(40) Kim, J.; Rana, A. S.; Kim, Y.; Kim, I.; Badloe, T.; Zubair, M.; Mehmood, M. Q.; Rho, J. Chiroptical Metasurfaces: Principles, Classification, and Applications. *Sensors* **2021**, *21*.

(41) Khaliq, H. S.; Nauman, A.; Lee, J.-W.; Kim, H.-R. Recent Progress on Plasmonic and

Dielectric Chiral Metasurfaces: Fundamentals, Design Strategies, and Implementation. *Advanced Optical Materials* 2023, *11*, 2300644.

(42) Mun, J.; Kim, M.; Yang, Y.; Badloe, T.; Ni, J.; Chen, Y.; Qiu, C.-W.; Rho, J. Electromagnetic chirality: from fundamentals to nontraditional chiroptical phenomena. *Light: Science & Applications* 2020, *9*, 139.

(43) Spreyer, F.; Mun, J.; Kim, H.; Kim, R. M.; Nam, K. T.; Rho, J.; Zentgraf, T. Second Harmonic Optical Circular Dichroism of Plasmonic Chiral Helicoid-III Nanoparticles. *ACS Photonics* 2022, *9*, 784–792, PMID: 35330905.

(44) Kakkar, T.; Keijzer, C.; Rodier, M.; Bukharova, T.; Taliansky, M.; Love, A. J.; Milner, J. J.; Karimullah, A. S.; Barron, L. D.; Gadegaard, N.; others Superchiral near fields detect virus structure. *Light: Science & Applications* 2020, *9*, 195.

(45) Kim, Y.; Kim, H.; Yang, Y.; Badloe, T.; Jeon, N.; Rho, J. Three-dimensional artificial chirality towards low-cost and ultra-sensitive enantioselective sensing. *Nanoscale* 2022, *14*, 3720–3730.

(46) Mao, L.; Cheng, P.; Liu, K.; Lian, M.; Cao, T. Sieving nanometer enantiomers using bound states in the continuum from the metasurface. *Nanoscale Adv.* 2022, *4*, 1617–1625.

(47) Lee, Y. H.; Won, Y.; Mun, J.; Lee, S.; Kim, Y.; Yeom, B.; Dou, L.; Rho, J.; Oh, J. H. Hierarchically manufactured chiral plasmonic nanostructures with gigantic chirality for polarized emission and information encryption. *Nature Communications* 2023, *14*, 7298.

(48) Huang, Z.; Wang, J.; Jia, W.; Zhang, S.; Zhou, C. Controllable perfect chiral optical response in planar metasurfaces empowered by quasi-bound states in the continuum. *Opt. Express* 2024, *32*, 33029–33041.

(49) Shi, T.; Deng, Z.-L.; Geng, G.; Zeng, X.; Zeng, Y.; Hu, G.; Overvig, A.; Li, J.; Qiu, C.-W.; Alù, A.; others Planar chiral metasurfaces with maximal and tunable chiroptical response driven by bound states in the continuum. *Nature Communications* 2022, *13*, 4111.

(50) Chen, Y.; Deng, H.; Sha, X.; Chen, W.; Wang, R.; Chen, Y.-H.; Wu, D.; Chu, J.; Kivshar, Y. S.; Xiao, S.; others Observation of intrinsic chiral bound states in the continuum. *Nature* 2023, *613*, 474–478.

(51) Dixon, J.; Lawrence, M.; Barton, D. R.; Dionne, J. Self-Isolated Raman Lasing with a Chiral Dielectric Metasurface. *Phys. Rev. Lett.* 2021, *126*, 123201.

(52) Lv, S.; Hu, F.; Luo, W.; Xu, H.; An, L. Design of tunable selective light-absorbing metasurfaces driven by intrinsically chiral quasi-bound states in the continuum. *Opt. Express* 2024, *32*, 30053–30064.

(53) Kühner, L.; Wendisch, F. J.; Antonov, A. A.; Bürger, J.; Hüttenhofer, L.; de S. Menezes, L.; Maier, S. A.; Gorkunov, M. V.; Kivshar, Y.; Tittl, A. Unlocking the out-of-plane dimension for photonic bound states in the continuum to achieve maximum optical chirality. *Light: Science & Applications* 2023, *12*, 250.

(54) Zhang, D.; Liu, T.; Lei, L.; Deng, W.; Wang, T.; Liao, Q.; Liu, W.; Xiao, S.; Yu, T. Tailoring intrinsic chirality in a two-dimensional planar waveguide grating via quasibound states in the continuum. *Physical Review B* 2024, *109*, 205403.

(55) Salzberg, C. D.; Villa, J. J. Infrared Refractive Indexes of Silicon Germanium and Modified Selenium Glass∗. *J. Opt. Soc. Am.* 1957, *47*, 244–246.

(56) Gurvitz, E. A.; Ladutenko, K. S.; Dergachev, P. A.; Evlyukhin, A. B.; Miroshnichenko, A. E.; Shalin, A. S. The high-order toroidal moments and anapole states in all-dielectric photonics. *Laser & Photonics Reviews* 2019, *13*, 1800266.

(57) Lepetit, T.; Kanté, B. Controlling multipolar radiation with symmetries for electromagnetic bound states in the continuum. *Physical Review B* 2014, *90*, 241103.

(58) Koshelev, K.; Lepeshov, S.; Liu, M.; Bogdanov, A.; Kivshar, Y. Asymmetric metasurfaces with high-Q resonances governed by bound states in the continuum. *Physical review letters* 2018, *121*, 193903.

(59) Sharma, S.; Lahiri, B.; Varshney, S. K. Accidental BIC in All-Dielectric Nano-Sized Tri-Air holes Silicon Disk Resonator. Conference on Lasers and Electro-Optics. 2022; p JTu3A.68.

(60) Hsu, C. W.; Zhen, B.; Lee, J.; Chua, S.-L.; Johnson, S. G.; Joannopoulos, J. D.; Soljačić, M. Observation of trapped light within the radiation continuum. *Nature* 2013, *499*, 188–191.

(61) Sadrieva, Z.; Frizyuk, K.; Petrov, M.; Kivshar, Y.; Bogdanov, A. Multipolar origin of bound states in the continuum. *Phys. Rev. B* 2019, *100*, 115303.

(62) Sadrieva, Z. F.; Sinev, I. S.; Koshelev, K. L.; Samusev, A.; Iorsh, I. V.; Takayama, O.; Malureanu, R.; Bogdanov, A. A.; Lavrinenko, A. V. Transition from Optical Bound States in the Continuum to Leaky Resonances: Role of Substrate and Roughness. *ACS Photonics* 2017, *4*, 723–727.

(63) Singh, R.; Al-Naib, I. A. I.; Yang, Y.; Roy Chowdhury, D.; Cao, W.; Rockstuhl, C.; Ozaki, T.; Morandotti, R.; Zhang, W. Observing metamaterial induced transparency in individual Fano resonators with broken symmetry. *Applied Physics Letters* 2011, *99*, 201107.

(64) Cong, L.; Singh, R. Symmetry-protected dual bound states in the continuum in metamaterials. *Advanced Optical Materials* 2019, *7*, 1900383.

(65) Wu, J.; Xu, X.; Su, X.; Zhao, S.; Wu, C.; Sun, Y.; Li, Y.; Wu, F.; Guo, Z.; Jiang, H.; Chen, H. Observation of Giant Extrinsic Chirality Empowered by Quasi-Bound States in the Continuum. *Phys. Rev. Appl.* **2021**, *16*, 064018.

(66) Gorkunov, M. V.; Antonov, A. A.; Tuz, V. R.; Kupriianov, A. S.; Kivshar, Y. S. Bound States in the Continuum Underpin Near-Lossless Maximum Chirality in Dielectric Metasurfaces. *Advanced Optical Materials* **2021**, *9*, 2100797.

TOC Graphic

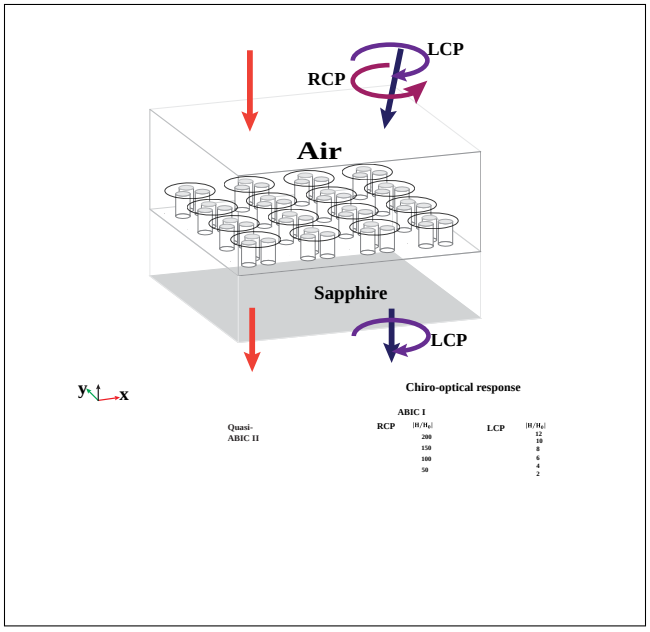
LCP
RCP
Air
Sapphire
LCP
y
x
Chiro-optical response
ABIC I
Quasi-
ABIC II
RCP
|R / R0|
200
150
100
50
LCP
|R / R0|
12
10
8
6
4
2